Moving obstacle potential in a spin-orbit-coupled Bose-Einstein condensate

Masaya Kato,[1] Xiao-Fei Zhang,[2,3,*] and Hiroki Saito[1,†]

[1]*Department of Engineering Science, University of Electro-Communications, Tokyo 182-8585, Japan*
[2]*Key Laboratory of Time and Frequency Primary Standards, National Time Service Center,*
Chinese Academy of Sciences, Xi'an 710600, China
[3]*School of Astronomy and Space Science, University of Chinese Academy of Sciences, Beijing 100049, China*

We investigate the dynamics around an obstacle potential moving in the plane-wave state of a pseudospin-1/2 Bose-Einstein condensate with Rashba spin-orbit coupling. We numerically investigate the dynamics of the system and find that it depends not only on the velocity of the obstacle but also significantly on the direction of obstacle motion, both of which are verified by the Bogoliubov analysis. The excitation diagram with respect to the velocity and direction is obtained. The dependence of the critical velocity on the strength of the spin-orbit coupling and the size of the obstacle is also investigated.

I. INTRODUCTION

The successful experimental realization of various synthetic gauge fields and spin-orbit coupling (SOC) in Bose-Einstein condensates (BECs) has recently drawn considerable theoretical attention [1–10], with a number of studies addressing the ground-state structures and static properties of topological excitations (for recent reviews, see, for example, Refs. [11–13]). Such synthetic gauge potentials in cold atoms are powerful tools for quantum many-body simulators of real materials. Moreover, the SO-coupled BEC exhibits numerous novel phases that cannot be found in conventional condensed-matter systems.

When an obstacle potential is moved in a superfluid, quantized vortices are created and released behind the obstacle potential above the critical velocity, which exerts drag force on the potential [14]. The dynamics of quantized vortices generated by moving obstacle potentials were recently observed experimentally [15–17]. For scalar BECs, a variety of phenomena in the BECs with moving obstacle potentials have been investigated: for example, vortex generation in trapped systems [18], scaling laws [19], three-dimensional dynamics [20,21], the Bénard–von Kármán vortex street [22–24], and hysteretic behaviors [25].

In the present paper, we focus on the problem of the moving obstacle potential in an SO-coupled BEC. The drag force on a moving impurity in a SO-coupled BEC has been calculated using the Bogoliubov spectrum [26,27]. In contrast, we directly solve the Gross-Pitaevskii (GP) equation with SOC and investigate the dynamical effects of the moving obstacle potential on the SO-coupled condensate. Most theoretical studies on BECs with Rashba SOC have focused on the static properties of the condensate [28–34], and there have only been a few studies on dynamics [35–38].

The dynamics of an SO-coupled BEC around a moving obstacle potential differs significantly from that of the usual scalar BEC in two ways. First, the ground state of the SO-coupled BEC breaks rotational symmetry, and the excitation spectrum above the ground state has an anisotropic characteristic form with a roton minimum [39–42]. Because of this feature, the Landau critical velocity and excitation properties depend on the direction of obstacle motion. Second, due to the close relationship between the spin and motional degrees of freedom, the dynamic properties of quantized vortices and solitons are dramatically altered by the SOC [43]. Consequently, the generation of vortices and waves around the moving obstacle potential is significantly affected by the SOC.

The remainder of the present paper is organized as follows. In Sec. II, we formulate the theoretical model for a moving obstacle potential in a uniform SO-coupled BEC. In Sec. III, the excitation dynamics induced by the obstacle potential and the Bogoliubov analysis are presented. The parameter dependence and velocity field are investigated in Secs. IV and V, respectively. Finally, in Sec. VI, the main results of the present paper are summarized.

II. FORMULATION OF THE PROBLEM

We consider a BEC of quasispin-1/2 atoms with Rashba SOC, where an obstacle potential is moving in a uniform system. The mean-field approximation is used, and the dynamics of the system is described by the GP equation as follows:

$$i\hbar \frac{\partial}{\partial t}\mathbf{\Psi} = -\frac{\hbar^2}{2m}\nabla^2\mathbf{\Psi} + i\frac{\hbar k_0}{m}\nabla \cdot \boldsymbol{\sigma}_\perp \mathbf{\Psi}$$
$$+ U(\boldsymbol{r},t)\mathbf{\Psi} + \hat{G}(\mathbf{\Psi},\mathbf{\Psi}^\dagger)\mathbf{\Psi}, \qquad (1)$$

where $\mathbf{\Psi}(\boldsymbol{r}) = (\psi_1(\boldsymbol{r}),\psi_2(\boldsymbol{r}))^T$ is the spinor order parameter, m is the mass of atoms, k_0 is the SOC coefficient, $\boldsymbol{\sigma}_\perp = (\sigma_x,\sigma_y,0)$ are 2×2 Pauli matrices, and $U(\boldsymbol{r},t)$ is a moving obstacle potential. The interaction matrix in Eq. (1) is given by

$$\hat{G}(\mathbf{\Psi},\mathbf{\Psi}^\dagger) = \begin{pmatrix} g_0|\psi_1|^2 & g_{12}|\psi_2|^2 \\ g_{12}|\psi_1|^2 & g_0|\psi_2|^2 \end{pmatrix}, \qquad (2)$$

where g_0 and g_{12} are the intra- and intercomponent interaction coefficients, respectively. (Here, we further assume that the two intracomponent interaction parameters are the same.) We consider an infinite system in which the atomic density $\mathbf{\Psi}^\dagger\mathbf{\Psi}$ far from the potential is constant, n_0. In the following,

*xfzhang@ntsc.ac.cn
†hiroki.saito@uec.ac.jp

we normalize the length and time by the healing length $\xi = \hbar/(g_0 n_0 m)$ and the characteristic time scale $\tau = \hbar/(g_0 n_0)$. In this unit, the wave function, velocity, and energy are normalized by $\sqrt{n_0}$, $\sqrt{g_0 n_0/m}$, and $g_0 n_0$. We transform Eq. (1) into a frame of reference that moves with the potential at velocity $\boldsymbol{v} = (v\cos\theta_v, v\sin\theta_v)$. The normalized GP equation becomes

$$i\frac{\partial\psi_1}{\partial t} = -\frac{1}{2}\nabla^2\psi_1 + i\kappa\partial_-\psi_2 + i\boldsymbol{v}\cdot\nabla\psi_1$$
$$+ V(\boldsymbol{r})\psi_1 + \left(|\psi_1|^2 + \gamma|\psi_2|^2\right)\psi_1, \qquad (3a)$$

$$i\frac{\partial\psi_2}{\partial t} = -\frac{1}{2}\nabla^2\psi_2 + i\kappa\partial_+\psi_1 + i\boldsymbol{v}\cdot\nabla\psi_2$$
$$+ V(\boldsymbol{r})\psi_2 + \left(\gamma|\psi_1|^2 + |\psi_2|^2\right)\psi_2, \qquad (3b)$$

where $\partial_\pm = \partial/\partial x \pm i\partial/\partial y$, $\kappa = k_0/\sqrt{g_0 n_0 m}$, and $\gamma = g_{12}/g_0$. We use a circular potential with radius R as

$$V(\boldsymbol{r}) = \begin{cases} V_0 & (|\boldsymbol{r}| \leqslant R) \\ 0 & (|\boldsymbol{r}| > R) \end{cases}, \qquad (4)$$

where the potential height V_0 is taken to be much larger than the chemical potential.

The ground state without the potential is the plane-wave state for $\gamma < 1$ and the stripe state for $\gamma > 1$. In the following discussion, we focus on the miscible case, $\gamma < 1$, and the ground state far from the potential is given by the plane-wave state, as follows:

$$\boldsymbol{\Psi}(\boldsymbol{r}) = \frac{1}{\sqrt{2}}\begin{pmatrix} e^{i\kappa x} \\ e^{i\kappa x} \end{pmatrix}, \qquad (5)$$

where the wave vector is chosen to be in the x direction.

We numerically solve Eq. (3) by the pseudospectral method using the fourth-order Runge-Kutta scheme. The initial state is the ground state with $\boldsymbol{v} = 0$, which is the plane-wave state in Eq. (5) far from the potential. The initial state is prepared by the imaginary-time propagation method, in which i on the left-hand side of Eq. (3) is replaced with -1. The numerical space is taken to be 400×400, which is sufficiently large, and the effect of the periodic boundary condition can be neglected.

III. EXCITATION INDUCED BY AN OBSTACLE

A. Dynamics of the system

First, we focus on the two special cases of $\theta_v = 0$ and π, where θ_v is the angle between the obstacle velocity $\boldsymbol{v}$ and the x axis. In the case of $\theta_v = 0$, when the velocity v exceeds a critical value, vortex-antivortex pairs are created, as shown in the upper left panel of Fig. 1(a). In this case, the periodic generation of vortex-antivortex pairs is, in a sense, reminiscent of the scalar case. However, the created vortex pairs are different from those in the scalar BEC, in that the vortex cores in both components deviate from each other, as shown in the lower panels of Fig. 1(a). Each component contains a vortex-antivortex pair, and vortex cores in one component are occupied by the other component, producing pairs of half-quantum vortices [43]. The upper right panel of Fig. 1(a) shows the drag force experienced by the obstacle, defined by $\boldsymbol{f} = i\partial_t \int d\boldsymbol{r}(\boldsymbol{\Psi}^\dagger \nabla\boldsymbol{\Psi})$. The drag force in the x direction exhibits periodic oscillation due to the periodic generation of
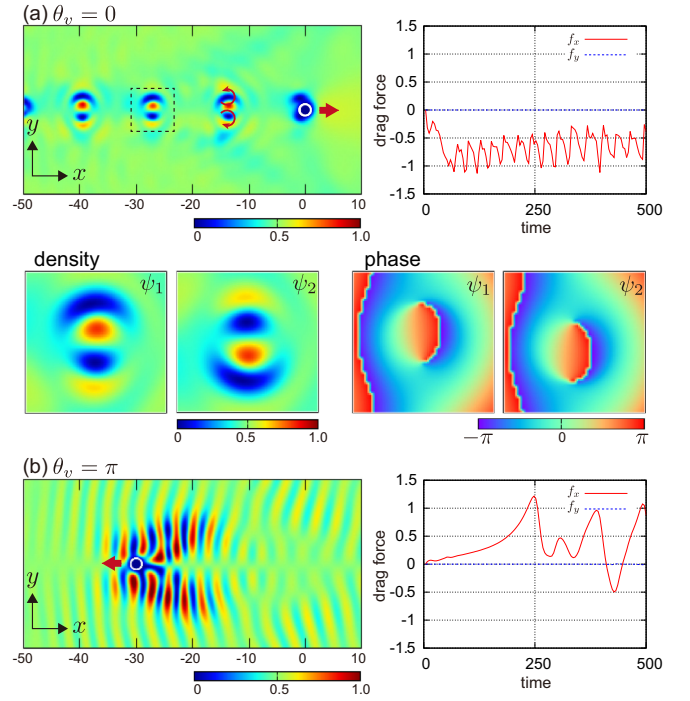

FIG. 1. (a) Snapshot of the density distribution $|\psi_1|^2$ (upper left panel) and time evolution of the drag force $\boldsymbol{f}$ exerted on the potential (upper right panel) for the velocity of the potential $(v,\theta_v) = (0.5,0)$. The density distributions, $|\psi_1|^2$ and $|\psi_2|^2$, and the phase distributions, $\arg\psi_1$ and $\arg\psi_2$, in the dashed square region are magnified into the lower panels. (b) $|\psi_1|^2$ and $\boldsymbol{f}$ for $(v,\theta_v) = (0.05,\pi)$. The white circles represent the obstacle potential, and the thick arrows indicate the moving direction. The curved arrows indicate the directions of the circulations of the vortices. The parameters are $R = 0.5$, $\kappa = 1$, and $\gamma = 0.8$. See Supplemental Material for movies of the dynamics of component 1 [44].

vortices, whereas the drag force in the y direction remains zero. In the case of $\theta_v = \pi$, when the velocity v exceeds a critical velocity, spin waves are excited, as shown in the left-hand panel of Fig. 1(b), which is very different from the case of $\theta_v = 0$. In this spin-wave state, high-density regions of components 1 and 2 are alternately aligned, as in the stripe state of an SOC BEC. The critical velocity of the spin-wave generation is much smaller than that of the vortex generation for $\theta_v = 0$. Thus, the excitation dynamics is strongly anisotropic with respect to the moving obstacle potential.

For a deeper understanding of the anisotropic properties, we explore the v and θ_v dependence of the dynamics. Figure 2 shows four typical dynamics with different velocities and azimuthal angles of the obstacle motion. These four kinds of dynamics are (I) weak excitation, (II) vortex pairs, (III) spin waves, and (IV) strong excitation. In the absence of excitation, the momentum-space distribution is $\delta(k_x - \kappa, k_y)$ due to the plane-wave background. For the weak excitation, no pronounced excitations are observed in the density distributions, but the long-wavelength excitations are induced at $k_x = \kappa$ and $|k_y| \lesssim 0.4$, as shown in Fig. 2(i). The density peak near the potential in Fig. 2(I) is due to the spin-dependent force by the SOC. For the spin wave, we find excitations at $\boldsymbol{k} \simeq -\kappa\boldsymbol{e}_x$, as shown in Fig. 2(iii). For the strong excitation, the
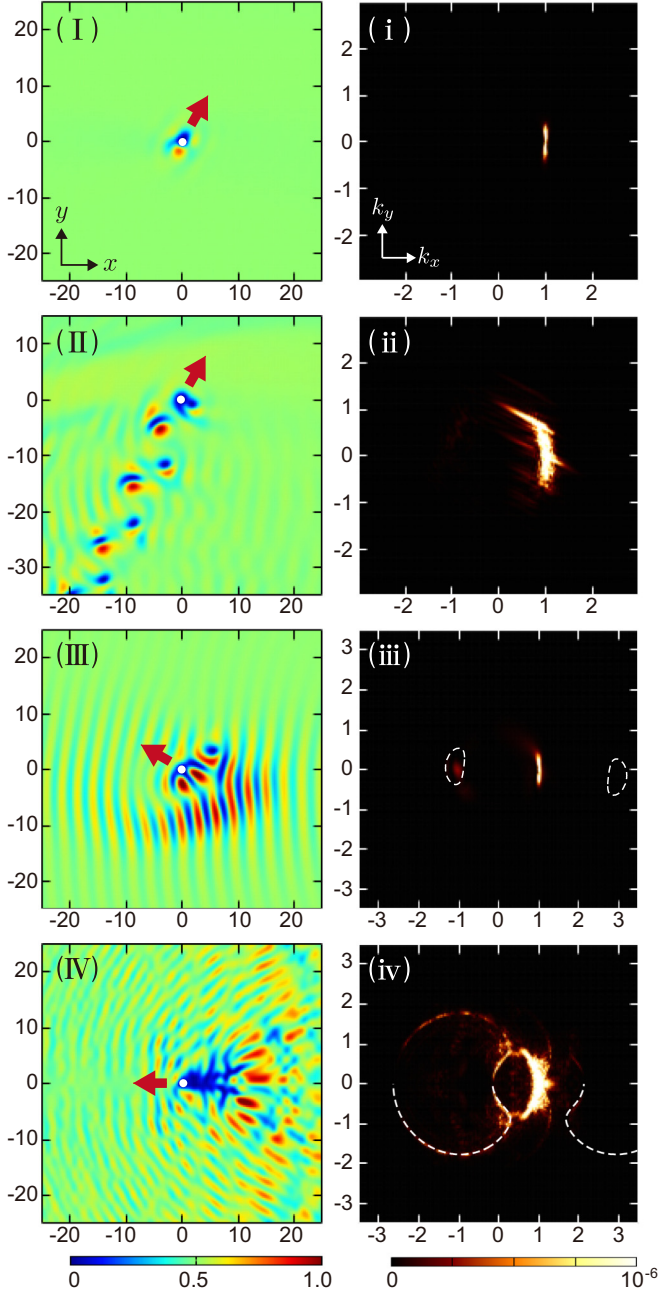
FIG. 2. Snapshots of (I–IV) the density distributions $|\psi_1|^2$ and (i–iv) the momentum-space distribution $|\tilde{\psi}_1|^2$ for $\kappa = 1$, $\gamma = 0.8$, and $R = 0.5$, where $\tilde{\psi}_1$ is the Fourier transform of ψ_1. (I, i) $(v, \theta_v) = (0.1, \pi/3)$. (II, ii) $(v, \theta_v) = (0.2, \pi/3)$. (III, iii) $(v, \theta_v) = (0.07, 5\pi/6)$. (IV, iv) $(v, \theta_v) = (0.4, \pi)$. The white solid circles and the red arrows in the left-hand panels are the obstacle potentials and moving directions, respectively. The dashed lines in (iii) and (iv) indicate the analytical solutions of $\omega(k_x - \kappa, k_y) = 0$ in Eq. (12). [In (iv), the dashed lines are shown only for $k_y < 0$.] See Supplemental Material for movies of the dynamics of $|\psi_1|^2$ and $|\tilde{\psi}_1|^2$ [44].

shock-wave pattern appears in the density distribution, as shown in Fig. 2(IV), which has a ring shape in the momentum space, as shown in Fig. 2(iv). These momentum-space behaviors are explained in Sec. III B. The movies in the Supplemental Material show these dynamics, where the initial
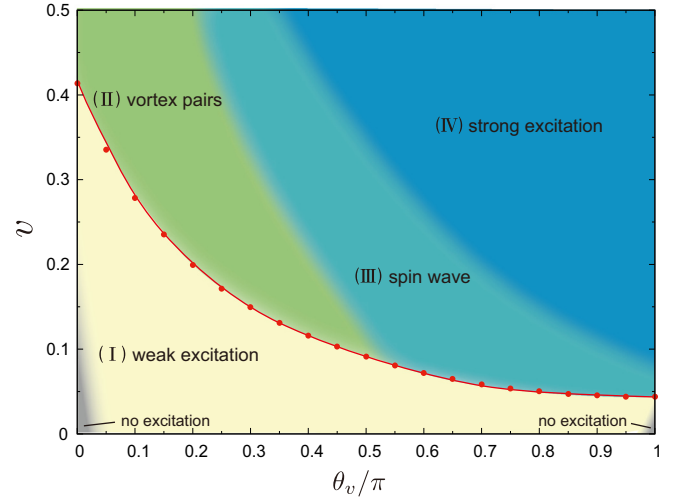

FIG. 3. The excitation diagram with respect to v and θ_v for $\kappa = 1$, $\gamma = 0.8$, and $R = 0.5$. The dynamics are classified into (I)–(IV), which correspond to those in Fig. 2. The red points indicate the critical velocity, at which the drag force increases suddenly, and the red line is a visual guide.

state is the ground state with $v = 0$, and v is suddenly changed at $t = 0$ [44].

Figure 3 shows a diagram of the four kinds of excitation with respect to v and θ_v, where regions I–IV correspond to the dynamics in Fig. 2. As v and θ_v are increased, the excitation behavior changes from region II to region IV. The boundaries between these three regions are vague. In contrast, there is a sharp boundary between region I and regions II–IV, as indicated by the red points in Fig. 3. When we start from region I and slowly increase the velocity v, the small drag force in region I steeply increases at this boundary. For small v and $\theta \simeq 0, \pi$, there are narrow regions in which the drag force almost vanishes, which are indicated by the dark regions in Fig. 3.

B. Bogoliubov analysis

We perform a Bogoliubov analysis in order to clarify the numerically obtained behavior. The wave function can be written as

$$\boldsymbol{\Psi}(\boldsymbol{r}, t) = e^{-i\mu t + i\kappa x} \left[\frac{1}{\sqrt{2}} \begin{pmatrix} 1 \\ 1 \end{pmatrix} + \delta\boldsymbol{\Psi}(\boldsymbol{r}, t) \right], \qquad (6)$$

where $\mu = -\kappa^2/2 - v_x\kappa + (1 + \gamma)/2$ is the chemical potential. The small excitation $\delta\boldsymbol{\Psi}(\boldsymbol{r}, t)$ is decomposed into

$$\delta\boldsymbol{\Psi}(\boldsymbol{r}, t) = \boldsymbol{\alpha} e^{i(\boldsymbol{q}\cdot\boldsymbol{r} - \omega t)} + \boldsymbol{\beta}^* e^{-i(\boldsymbol{q}\cdot\boldsymbol{r} - \omega t)}, \qquad (7)$$

where $\boldsymbol{\alpha} = (\alpha_1, \alpha_2)^{\mathrm{T}}$ and $\boldsymbol{\beta} = (\beta_1, \beta_2)^{\mathrm{T}}$ are the amplitudes, $\boldsymbol{q} = (q\cos\theta_q, q\sin\theta_q)$ is the wave number, and ω is the frequency of the excitation. Substituting Eq. (6) into Eq. (3) with $V = 0$ and taking the first order of $\delta\boldsymbol{\Psi}$, we obtain

$$\left(\mu' + i\frac{\partial}{\partial t}\right)\delta\boldsymbol{\Psi} = (\mathcal{H}_0 + \mathcal{H}_1)\delta\boldsymbol{\Psi} + \mathcal{H}_2\delta\boldsymbol{\Psi}^* + i\boldsymbol{v}\cdot\nabla\delta\boldsymbol{\Psi}, \qquad (8)$$
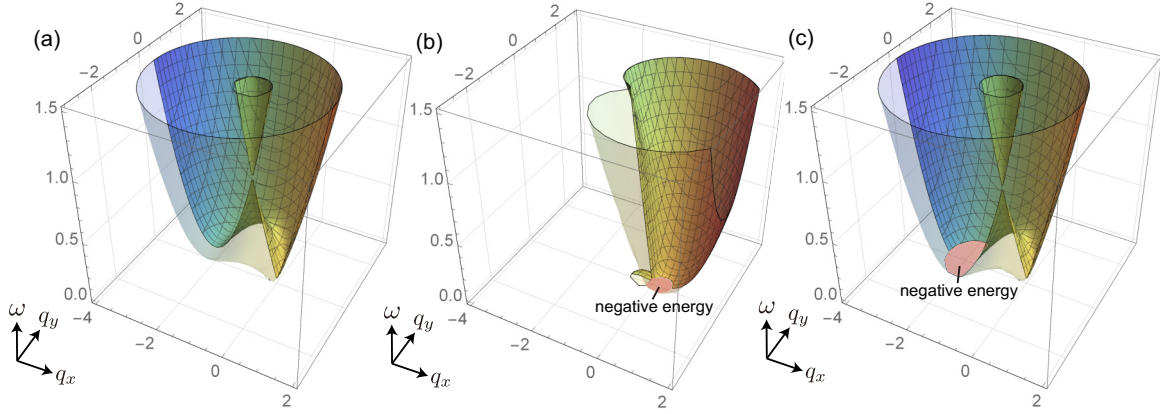
FIG. 4. Excitation spectrum of a uniform system for $\kappa = 1$ and $\gamma = 0.8$ in the frame moving at velocities (a) $(v,\theta_v) = (0,0)$, (b) $(v,\theta_v) = (1,0)$, and (c) $(v,\theta_v) = (0.1,\pi)$. The colored regions on the q_x-q_y plane indicate negative energy, $\omega(\boldsymbol{q}) < 0$.

where $\mu' = -\kappa^2/2 + (1+\gamma)/2$,

$$\mathcal{H}_0 = \begin{pmatrix} -\frac{1}{2}(\nabla + i\kappa \boldsymbol{e}_x)^2 & i\kappa\partial_- - \kappa^2 \\ i\kappa\partial_+ - \kappa^2 & -\frac{1}{2}(\nabla + i\kappa \boldsymbol{e}_x)^2 \end{pmatrix}, \tag{9}$$

and

$$\mathcal{H}_1 = \frac{1}{2}\begin{pmatrix} 2+\gamma & \gamma \\ \gamma & 2+\gamma \end{pmatrix}, \quad \mathcal{H}_2 = \frac{1}{2}\begin{pmatrix} 1 & \gamma \\ \gamma & 1 \end{pmatrix}. \tag{10}$$

The Bogoliubov equation is obtained from Eqs. (7)–(10) as $\{\mathcal{H}(\boldsymbol{q}) - [\omega(\boldsymbol{q}) + \boldsymbol{v} \cdot \boldsymbol{q}]\mathcal{I}\}\boldsymbol{\chi} = \boldsymbol{0}$, where

$$\mathcal{H}(\boldsymbol{q}) = \begin{pmatrix} \frac{1}{2}q^2 + \kappa q_x + \kappa^2 + \frac{1}{2} & -\kappa q_- - \kappa^2 + \frac{1}{2}\gamma & \frac{1}{2} & \frac{1}{2}\gamma \\ -\kappa q_+ - \kappa^2 + \frac{1}{2}\gamma & \frac{1}{2}q^2 + \kappa q_x + \kappa^2 + \frac{1}{2} & \frac{1}{2}\gamma & \frac{1}{2} \\ -\frac{1}{2} & -\frac{1}{2}\gamma & -\frac{1}{2}q^2 + \kappa q_x - \kappa^2 - \frac{1}{2} & -\kappa q_+ + \kappa^2 - \frac{1}{2}\gamma \\ -\frac{1}{2}\gamma & -\frac{1}{2} & -\kappa q_- + \kappa^2 - \frac{1}{2}\gamma & -\frac{1}{2}q^2 + \kappa q_x - \kappa^2 - \frac{1}{2} \end{pmatrix} \tag{11}$$

and $\boldsymbol{\chi} = (\alpha_1,\alpha_2,\beta_1,\beta_2)^{\mathrm{T}}$. The Bogoliubov excitation spectrum $\omega(\boldsymbol{q},\boldsymbol{v})$ is the solution of

$$|\mathcal{H}(\boldsymbol{q}) - (\omega + \boldsymbol{v} \cdot \boldsymbol{q})\mathcal{I}| = 0. \tag{12}$$

Figure 4(a) shows the excitation spectrum $\omega(\boldsymbol{q},\boldsymbol{v})$ at $\boldsymbol{v} = \boldsymbol{0}$. The spectrum breaks the rotational symmetry and has a rotonlike minimum at $q_y < 0$. For nonzero v, a region in which ω becomes negative appears. The Landau critical velocity is defined as the velocity above which the negative-ω region appears on the q_x-q_y plane. Thus, in the present case, the Landau critical velocity depends on the angle θ_v of the moving potential. When $\theta_v = 0$, the negative-energy region is located near the origin of the momentum space, as shown in Fig. 4(b), which is similar to the case of a scalar BEC. For $\theta_v = \pi$, on the other hand, the negative-energy region appears at finite momentum due to the rotonlike minimum, as shown in Fig. 4(c). This corresponds to the spin-wave excitation in Figs. 2(III) and 2(iii).

Setting $\omega = 0$ in Eq. (12), we have

$$|\mathcal{H}(\boldsymbol{q}) - \boldsymbol{v} \cdot \boldsymbol{q}\mathcal{I}| = 0. \tag{13}$$

For given θ_v, the Landau critical velocity v_L is the minimum value of $v \geqslant 0$ for which Eq. (13) has at least a real solution $\boldsymbol{q}$. First, we solve Eq. (13) under the assumption that the solution

is $q \simeq 0$. Taking the limit $q \to 0$, Eq. (13) is rewritten as

$$v = \sqrt{\frac{1+\gamma}{2}} \left| \frac{\cos\theta_q}{\cos(\theta_q - \theta_v)} \right|, \tag{14}$$

where θ_q is the azimuthal angle in the q_x-q_y plane. When $\theta_v \neq 0$ and π, the minimum value of $v \geqslant 0$ for which Eq. (14) has a solution is $v = 0$ (the solution is $\theta_q = \pm\pi/2$). Thus, the Landau critical velocity for $\theta_v \neq 0$ and π is $v_L = 0$. The instability around $\theta_q = \pm\pi/2$ appears in Fig. 2(i). The Landau critical velocities for $\theta_v = 0$ and π are obtained analytically, and we have

$$v_L(\theta_v) = \begin{cases} \sqrt{(1+\gamma)/2} & (\theta_v = 0) \\ -\kappa + \sqrt{\kappa^2 + (1-\gamma)/2} & (\theta_v = \pi). \\ 0 & (\text{other}) \end{cases} \tag{15}$$

Note that v_L for $\theta_v = 0$ is independent of κ, which has a phononlike relation $\omega \propto q_x$ for $q_x \ll 1$, as in the Bogoliubov mode of a scalar BEC. When $\theta_v = \pi$, the wave number

$$q_x = -\sqrt[4]{8\kappa^2(1-\gamma+2\kappa^2)} \tag{16}$$

first becomes negative above the Landau critical velocity, which corresponds to the wave number for the spin wave shown in Figs. 2(III) and 2(iii). In the limit of $\kappa \to 0$, the

two velocities in Eq. (15) are $\sqrt{(1 \pm \gamma)/2}$, which agree with those in the two-component BEC without SO coupling [45].

Although the Landau critical velocity is zero for $\theta_v \neq 0$ and π in Eq. (15), the effect of the excitation remains slight when v is small, as shown in Figs. 2(I) and 2(i). However, there exists an effective critical velocity, above which the drag force suddenly increases, as indicated by the red line in Fig. 3.

The dashed lines in Figs. 2(iii) and 2(iv) indicate the analytical solutions of $\omega(k_x - \kappa, k_y, v) = 0$ for $(v, \theta_v) = (0.07, 5\pi/6)$ and $(v, \theta_v) = (0.4, \pi)$, respectively. In Fig. 2(iii), condensates are excited in the region of $\omega(k_x - \kappa, k_y, v) < 0$. For the much larger velocity, a ring excitation appears in the momentum space, which we classified into (IV) strong excitation. Due to the energy conservation law, the entire region of $\omega(k_x - \kappa, k_y, v) < 0$ inside the dashed line in Fig. 2(iv) cannot be excited, and only the ringlike region at $\omega(k_x - \kappa, k_y, v) \simeq 0$ is excited.

For $\theta_v = 0$ and π, Eq. (11) can be diagonalized, and the eigenvectors can be obtained. For $\theta_v = 0$, the eigenvector is

$$\boldsymbol{\alpha}(q) \propto \sqrt{1 + f(q)} \begin{pmatrix} 1 \\ 1 \end{pmatrix}, \tag{17a}$$

$$\boldsymbol{\beta}(q) \propto -\sqrt{1 - f(q)} \begin{pmatrix} 1 \\ 1 \end{pmatrix}, \tag{17b}$$

where

$$f(q) = \frac{q\sqrt{q^2 + 2(1 + \gamma)}}{q^2 + 1 + \gamma}, \tag{18}$$

and for $\theta_v = \pi$,

$$\boldsymbol{\alpha}(q) \propto \sqrt{1 + g(q)} \begin{pmatrix} 1 \\ -1 \end{pmatrix}, \tag{19a}$$

$$\boldsymbol{\beta}(q) \propto \sqrt{1 - g(q)} \begin{pmatrix} -1 \\ 1 \end{pmatrix}, \tag{19b}$$

where

$$g(q) = \frac{\sqrt{(q^2 + 4\kappa^2)(q^2 + 4\kappa^2 + 2 - 2\gamma)}}{q^2 + 4\kappa^2 + 1 - \gamma}. \tag{20}$$

In the case of $\gamma \simeq 1$, we find $|\boldsymbol{\beta}|/|\boldsymbol{\alpha}| \simeq 0$ in $\theta_v = \pi$. This is why the Bogoliubov counterparts [right-hand side dashed lines in Figs. 2(iii) and 2(vi)] are not significantly excited.

IV. PARAMETER DEPENDENCE OF THE CRITICAL VELOCITY

Next, we discuss the dependence of the critical velocity on the SO-coupling strength κ and on the obstacle radius R. We focus on the moving directions $\theta_v = 0$ and π of the obstacle potential. The critical velocity v_c is defined as the velocity above which the drag force suddenly increases, as indicated by the red line in Fig. 3.

Figure 5 shows the κ dependence of the critical velocity v_c. For $\theta_v = 0$, v_c discontinuously decreases at $\kappa \simeq 0.03$, and gradually decreases with an increase in κ. The discontinuous change is attributed to the $\psi_1 - \psi_2$ symmetry breaking in the
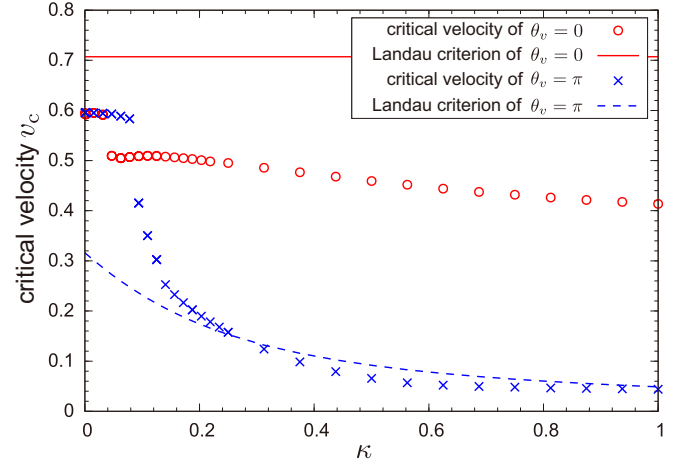

FIG. 5. Dependence of the critical velocity v_c on the strength of the SO coupling κ for $\gamma = 0.8$ and $R = 0.5$. The red circles and blue crosses indicate the critical velocities for $\theta_v = 0$ and π, respectively. The red solid line and the blue dashed line indicate the Landau criterion for $\theta_v = 0$ and π, respectively, in Eq. (15).

vortices that are generated by the potential. For $\kappa \gtrsim 0.03$, the vortex cores in the two components are displaced from each other [43], which can be regarded as a pair of half-quantized vortices, whereas the vortices generated for $\kappa \lesssim 0.03$ are the usual topological defects of the global phase in which $\psi_1 = \psi_2$ is preserved. Similarly, for $\theta_v = \pi$, the symmetry between the two components is broken for $\kappa \gtrsim 0.08$, causing the sudden change in v_L. The critical velocity v_c is below the Landau critical velocity v_L for $\kappa \gtrsim 0.3$. The deviation of the critical velocities from the Landau criteria in Fig. 5 may be due to the finite-size effect of the obstacle potential, since a finite-size obstacle modifies the flow pattern and excitation spectrum around it.

Figure 6 shows the dependence of critical velocity v_c on the obstacle radius R for $\theta_v = 0$ and π. The critical velocity for
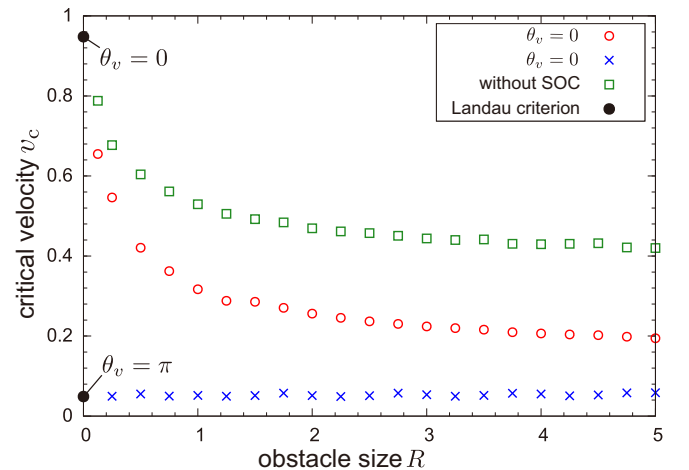

FIG. 6. Dependence of critical velocities v_c on the obstacle radius R for $\kappa = 1$ and $\gamma = 0.8$. The red circles and blue crosses indicate the critical velocities for $\theta_v = 0$ and π, respectively. The green squares indicate the critical velocity without the SOC. The black solid circles indicate the Landau criteria in Eq. (15).
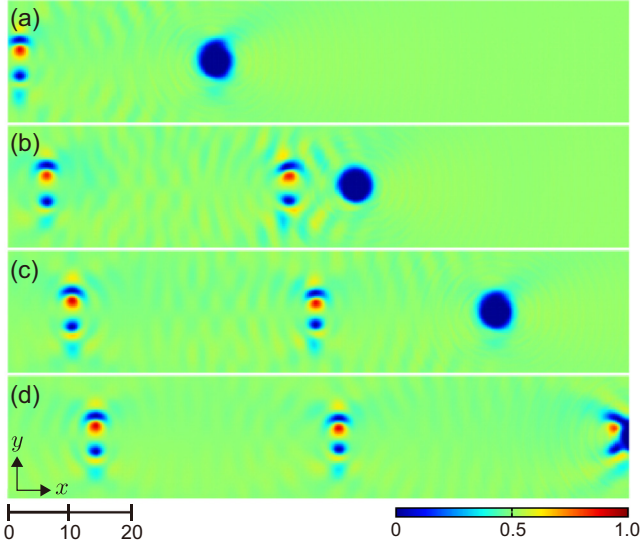
FIG. 7. Serial snapshots of the density distributions $|\psi_1|^2$ of the dynamics in the rest frame for $\kappa = 1$ and $\gamma = 0.8$. The velocity of the moving obstacle is $(v, \theta_v) = (0.5, 0)$, and the radius is $R = 2$. The time interval is 75, and the field of view is 100×20. See Supplemental Material for movies of the dynamics of component 1 [44].

the system without the SOC is also plotted for comparison. In the limit of small R, the critical velocities approach the Landau critical velocity, as expected. The critical velocity with SOC is always smaller than that without the SOC, for the same reason that the steep decrease of v_c occurs in Fig. 5, i.e., the symmetry breaking between the two components due to the spin-dependent force by the SOC tends to decrease the critical velocity. Interestingly, for the case of $\theta_v = \pi$, v_c is approximately independent of R, whereas v_c decreases with R for the case of $\theta_v = 0$.

Figure 7 shows serial snapshots of the density distribution in the rest frame for $(v, \theta_v) = (0.5, 0)$. The velocity of the vortex pairs released from the moving obstacle potential, $v_{\text{vortex}} \simeq 0.05$, is much smaller than that without the SOC [43]. In the rest frame, the vortex pairs are created just like a moving obstacle would leave behind them on its trajectory.

V. VELOCITY FIELD

Finally, we discuss the velocity field distribution induced by the obstacle potential. The velocity field of the condensate is defined as

$$\boldsymbol{v}_f(\boldsymbol{r}) = \frac{1}{2i\rho}[\boldsymbol{\Psi}^\dagger \nabla \boldsymbol{\Psi} - \boldsymbol{\Psi}^T \nabla \boldsymbol{\Psi}^*] - \frac{\kappa}{\rho} \boldsymbol{\Psi}^\dagger \boldsymbol{\sigma}_\perp \boldsymbol{\Psi}, \quad (21)$$

where $\rho = |\psi_1|^2 + |\psi_2|^2$. The first term on the right-hand side of Eq. (21) is the usual superfluid velocity, and the second term originates from the SOC. The velocity field satisfies the equation of continuity, $\partial \rho / \partial t + \nabla \cdot (\rho \boldsymbol{v}) = 0$. The velocity field far from the obstacle potential vanishes due to the cancellation between the first and second terms of Eq. (21).

Figures 8(a) and 8(b) show the velocity field of the ground state with the obstacle potential at rest. Even for the static case, the velocity field exhibits complicated structures containing multiple circulations. A strong rightward flow is observed in
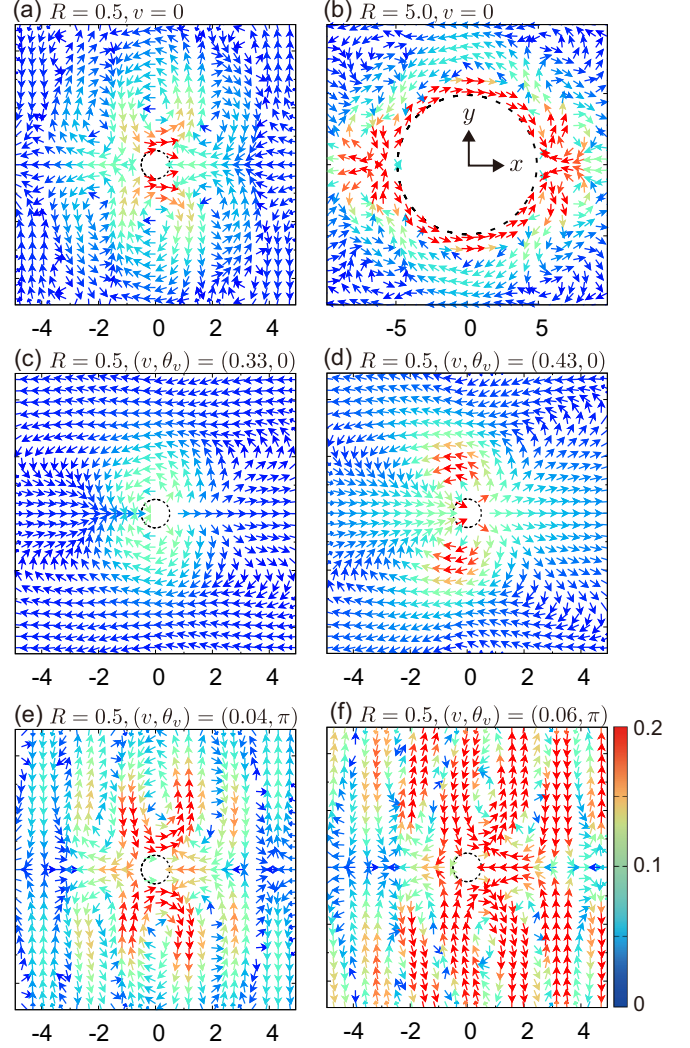

FIG. 8. Velocity field distribution induced by an obstacle potential for $\kappa = 1$ and $\gamma = 0.8$. (a, b) Ground states with the obstacle potential at rest. The radii of the circular potential are $R = 0.5$ and 5.0. The velocity of the potential with radius $R = 0.5$ is increased as $v(t) = 6.0 \times 10^{-4} t$ in (c) and (d) and $v(t) = -7.0 \times 10^{-5} t$ in (e) and (d). (c) $(v, \theta_v) = (0.33, 0)$ at $t = 550$. (d) $(v, \theta_v) = (0.43, 0)$ at $t = 717$. (e) $(v, \theta_v) = (0.04, \pi)$ at $t = 600$. (f) $(v, \theta_v) = (0.06, \pi)$ at $t = 835$. The arrows indicate the direction of the velocity field, and their color indicates the value of v. The dashed circle in each panel indicates the obstacle potential.

the vicinity of the potential, which is explained as follows. The spin-dependent SOC forces on components 1 and 2 are in the $+y$ and $-y$ directions, respectively, which results in the density difference between the two components at the edge of the potential. For the wave function,

$$\boldsymbol{\Psi}(\boldsymbol{r}) = \begin{pmatrix} u_1(\boldsymbol{r}) e^{i\kappa x} \\ u_2(\boldsymbol{r}) e^{i\kappa x} \end{pmatrix}, \quad (22)$$

with real functions u_1 and u_2, the velocity field is given by $\boldsymbol{v}_f = \kappa \rho^{-1}(u_1 - u_2)^2 \boldsymbol{e}_x$, where $\boldsymbol{e}_x$ is the unit vector in the x direction. Thus, the density imbalance at the edge of the potential generates the rightward velocity field.

For $\theta_v = 0$, as the obstacle velocity increases, the circulations in the velocity field vanish and the velocity field becomes similar to that for the system without SOC, as shown in Figs. 8(c) and 8(d). The disappearance of the complicated velocity field is due to the disappearance of the imbalance between $|\psi_1|^2$ and $|\psi_2|^2$ by the fast motion of the obstacle.

On the other hand, the velocity field for $\theta_v = \pi$ is quite different from the case of $\theta_v = 0$, as shown in Figs. 8(e) and 8(f). In this case, the flows are mainly along the y direction, and alternately shift upward and downward. This behavior can be understood based on the results of the Bogoliubov analysis in Sec. III B. Assuming $\gamma = 1$, for simplicity, the most unstable wave number is estimated to be $\boldsymbol{q} \simeq -2\kappa \boldsymbol{e}_x$ from Eq. (16), and the eigenvector in Eq. (19) is approximated to be $\boldsymbol{\alpha} \propto (1, -1)^T$ and $\boldsymbol{\beta} \simeq \boldsymbol{0}$. Substituting these into Eq. (6), the excited wave function becomes

$$\Psi(\boldsymbol{r},t) = \frac{e^{-i\mu t}}{\sqrt{2}}\left[\begin{pmatrix}1\\1\end{pmatrix}e^{i\kappa x} + \delta u \begin{pmatrix}1\\-1\end{pmatrix}e^{-i\kappa x}\right], \qquad (23)$$

where δu is an infinitesimal amplitude of the excitation, which is assumed to be real without loss of generality. The velocity field in Eq. (21) is thus obtained as

$$\boldsymbol{v}_f(\boldsymbol{r}) = -2\delta u \sin(2\kappa x)\boldsymbol{e}_y, \qquad (24)$$

where $\boldsymbol{e}_y$ is a unit vector in the y direction. In Fig. 8(f), the wavelength of the velocity field is estimated to be $\lambda_v \simeq 3$, which agrees well with the wavelength π/κ in Eq. (24).

VI. CONCLUSIONS

In conclusion, we have investigated the dynamics of an SO-coupled BEC with a moving obstacle potential. We found that the obstacle potential moving in the plane-wave state exhibits a variety of excitation dynamics. We have shown that the dynamics strongly depend on the direction of the obstacle motion. When the potential moves in the plane-wave direction, half-quantized vortex pairs are released. When the potential moves in the opposite direction, on the other hand, spin waves are dominant. This behavior can be understood from the Bogoliubov spectrum. Although the Landau critical velocity derived from the Bogoliubov spectrum is zero for the other directions, we numerically found that there is an effective critical velocity, below which excitation is negligible and above which the drag force on the obstacle increases steeply. We obtained a diagram of the excitation behavior with respect to the velocity $\boldsymbol{v}$ of the potential. We explored the dependence of the effective critical velocity on the strength of the SO coupling κ and the obstacle size R. We also investigated the velocity field distribution for the system, which exhibits complicated flow patterns depending on the parameters.

[1] Y.-J. Lin, R. L. Compton, K. Jiménez-García, J. V. Porto, and I. B. Spielman, Nature (London) **462**, 628 (2009).

[2] Y.-J. Lin, K. Jiménez-García, and I. B. Spielman, Nature (London) **471**, 83 (2011).

[3] Y.-J. Lin, R. L. Compton, K. Jiménez-García, W. D. Phillips, J. V. Porto, and I. B. Spielman, Nat. Phys. **7**, 531 (2011).

[4] Y.-J. Lin, R. L. Compton, A. R. Perry, W. D. Phillips, J. V. Porto, and I. B. Spielman, Phys. Rev. Lett. **102**, 130401 (2009).

[5] B. M. Anderson, G. Juzeliūnas, V. M. Galitski, and I. B. Spielman, Phys. Rev. Lett. **108**, 235301 (2012).

[6] Z. Fu, L. Huang, Z. Meng, P. Wang, L. Zhang, S. Zhang, H. Zhai, P. Zhang, and J. Zhang, Nat. Phys. **10**, 110 (2014).

[7] L. Huang, Z. Meng, P. Wang, P. Peng, S.-L. Zhang, L. Chen, D. Li, Q. Zhou, and J. Zhang, Nat. Phys. **12**, 540 (2016).

[8] Z. M. Meng, L. H. Huang, P. Peng, D. H. Li, L. C. Chen, Y. Xu, C. Zhang, P. Wang, and J. Zhang, Phys. Rev. Lett. **117**, 235304 (2016).

[9] S. C. Ji, J. Y. Zhang, L. Zhang, Z. D. Du, W. Zheng, Y. J. Deng, H. Zhai, S. Chen, and J. W. Pan, Nat. Phys. **10**, 314 (2014).

[10] Z. Wu, L. Zhang, W. Sun, X.-T. Xu, B.-Z. Wang, S.-C. Ji, Y. Deng, S. Chen, X.-J. Liu, and J.-W. Pan, Science **354**, 83 (2016).

[11] J. Dalibard, F. Gerbier, G. Juzeliūnas, and P. Öhberg, Rev. Mod. Phys. **83**, 1523 (2011).

[12] N. Goldman, G. Juzeliūnas, P. Öhberg, and I. B. Spielman, Rep. Prog. Phys. **77**, 126401 (2014).

[13] H. Zhai, Rep. Prog. Phys. **78**, 026001 (2015).

[14] T. Frisch, Y. Pomeau, and S. Rica, Phys. Rev. Lett. **69**, 1644 (1992).

[15] T. W. Neely, E. C. Samson, A. S. Bradley, M. J. Davis, and B. P. Anderson, Phys. Rev. Lett. **104**, 160401 (2010).

[16] W. J. Kwon, S. W. Seo, and Y. I. Shin, Phys. Rev. A **92**, 033613 (2015).

[17] W. J. Kwon, J. H. Kim, S. W. Seo, and Y. Shin, Phys. Rev. Lett. **117**, 245301 (2016).

[18] B. Jackson, J. F. McCann, and C. S. Adams, Phys. Rev. Lett. **80**, 3903 (1998).

[19] C. Huepe and M. E. Brachet, Physica D **140**, 126 (2000).

[20] C. Nore, C. Huepe, and M. E. Brachet, Phys. Rev. Lett. **84**, 2191 (2000).

[21] A. Aftalion, Q. Du, and Y. Pomeau, Phys. Rev. Lett. **91**, 090407 (2003).

[22] K. Sasaki, N. Suzuki, and H. Saito, Phys. Rev. Lett. **104**, 150404 (2010).

[23] G. W. Stagg, N. G. Parker, and C. F. Barenghi, J. Phys. B **47**, 095304 (2014).

[24] M. T. Reeves, T. P. Billam, B. P. Anderson, and A. S. Bradley, Phys. Rev. Lett. **114**, 155302 (2015).

[25] T. Kadokura, J. Yoshida, and H. Saito, Phys. Rev. A **90**, 013612 (2014).

[26] P.-S. He, Y.-H. Zhu, and W.-M. Liu, Phys. Rev. A **89**, 053615 (2014).

[27] R. Liao, O. Fialko, J. Brand, and U. Zülicke, Phys. Rev. A **93**, 023625 (2016).

[28] C. Wang, C. Gao, C.-M. Jian, and H. Zhai, Phys. Rev. Lett. **105**, 160403 (2010).

[29] T.-L. Ho and S. Zhang, Phys. Rev. Lett. **107**, 150403 (2011).

[30] X. F. Zhou, J. Zhou, and C. J. Wu, Phys. Rev. A **84**, 063624 (2011).

[31] S. Sinha, R. Nath, and L. Santos, Phys. Rev. Lett. **107**, 270401 (2011).

[32] H. Hu, B. Ramachandhran, H. Pu, and X.-J. Liu, Phys. Rev. Lett. **108**, 010402 (2012).

[33] T. Kawakami, T. Mizushima, M. Nitta, and K. Machida, Phys. Rev. Lett. **109**, 015301 (2012).

[34] B. Ramachandhran, B. Opanchuk, X.-J. Liu, H. Pu, P. D. Drummond, and H. Hu, Phys. Rev. A **85**, 023606 (2012).

[35] J. Radić, T. A. Sedrakyan, I. B. Spielman, and V. Galitski, Phys. Rev. A **84**, 063604 (2011).

[36] A. L. Fetter, Phys. Rev. A **89**, 023629 (2014).

[37] K. Kasamatsu, Phys. Rev. A **92**, 063608 (2015).

[38] A. Gallemí, M. Guilleumas, R. Mayol, and A. M. Mateo, Phys. Rev. A **93**, 033618 (2016).

[39] Q. Zhu, C. Zhang, and B. Wu, Europhys. Lett. **100**, 50003 (2012).

[40] M. A. Khamehchi, Y. Zhang, C. Hamner, T. Busch, and P. Engels, Phys. Rev. A **90**, 063624 (2014).

[41] S. C. Ji, L. Zhang, X. T. Xu, Z. Wu, Y. Deng, S. Chen, and J. W. Pan, Phys. Rev. Lett. **114**, 105301 (2015).

[42] K. Sun, C. Qu, Y. Xu, Y. Zhang, and C. Zhang, Phys. Rev. A **93**, 023615 (2016).

[43] M. Kato, X.-F. Zhang, and H. Saito, Phys. Rev. A **95**, 043605 (2017).

[44] See Supplemental Material at http://link.aps.org/supplemental/10.1103/PhysRevA.96.033613 for movies of the dynamics.

[45] E. V. Goldstein and P. Meystre, Phys. Rev. A **55**, 2935 (1997).